UNIVERSITAT DE BARCELONA

ICFO

Master in Quantum Science and Technology

Master Thesis

A Strontium Atomic Source for Ultracold Quantum Gas Experiments

Author: Eric Gil Portal

Barcelona, 29th August, 2022

Supervisor:	Prof. Dr. Leticia Tarruell
Co-supervisor:	Dr. Antonio Rubio Abadal
Institution:	ICFO - Institut de Ciències Fotòniques

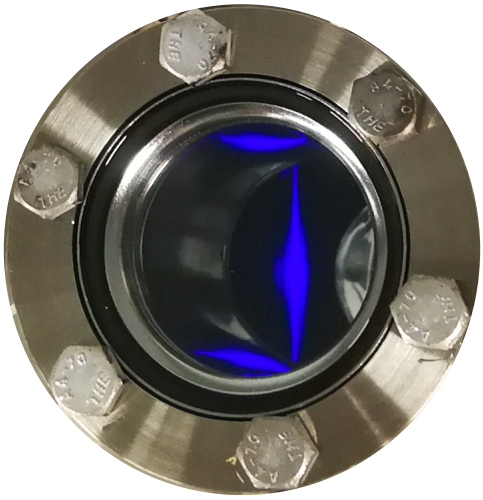

A Strontium Atomic Source for Ultracold Quantum Gas Experiments

Eric Gil Portal

Supervised by: Dr. Antonio Rubio Abadal, Prof. Dr. Leticia Tarruell

ICFO - Institut de Ciencies Fotoniques, The Barcelona Institute of Science and Technology, 08860 Castelldefels (Barcelona), Spain

29 August 2022

Abstract: In this work we report on the construction and characterization of a strontium atomic source that will be used as a first step in the production of ultracold quantum gases. We detail the design and assembly of the atomic oven, as well as the vacuum chamber and the optical setup built for its study. We also present the results of spectroscopy measurements using quasi-resonant laser light, from which we infer information about the density and velocity profiles of the atomic beam. Finally, we implement a one-dimensional transverse cooling to enhance the collimation of the atomic beam, demonstrating an increase in the resulting atomic density.

Keywords: Cold atoms, strontium, atomic oven, laser cooling.

Acknowledgements: First and foremost I want to express my gratitude to my supervisors: Toni, for being a fundamental guide throughout my thrilling discovery of experimental physics, and Leticia, for your always passionate support and advise. I am also profoundly thankful to the rest of the strontium team: Vasiliy, Jonatan, Sandra, Roland and Carla. It has been a pleasure learning from you every day and every time you helped me. Next, I wish to thank the members of the potassium team: Ramón, Craig, Sofie and especially Ana for accompanying me during all the hours we spent together in the lab. I would also like to thank the members of the theory team, and in particular Julia and Claudio. Last but by no means least, I want to thank those others who, at ICFO and beyond, have filled with shine my time here.

Eric Gil Portal: ericgilportal@gmail.com

Contents

1 Introduction

Condensed matter physics is one of the most actives areas of modern physics due to the rich diversity of phenomena encompassed and their many potential applications. Nevertheless, the complexity of the laws of quantum mechanics that govern the collective effects subjected to study entails that many crucial problems in this field remain incompletely understood. Conventional computers, that are essential to understand classical systems for which no analytical description has been achieved, are unsuitable for simulating the quantum many-body systems involved. The Hilbert space becomes too large for direct numerical simulation, as the number of complex amplitudes needed to describe the system increases exponentially with the number of particles.

To overcome this problem, the idea of a *quantum simulator* [Fey82, GAN13] arose: a highly controllable and tunable quantum system which is able to reproduce the behaviour of a theoretical system described by the Hamiltonian we want to study. Among other experimental platforms, *ultracold quantum gases* [BDN12] have proven to possess these characteristics, being able to, for instance, simulate the theoretical behaviour of electrons in solids, where these are replaced by fermionic atoms and the crystalline structure is emulated with interfering laser beams. This opens the possibility of exploring key but poorly-understood regimes like high-temperature superconductivity in a precisely controlled environment.

Some examples of successfully realized solid state Hamiltonians include bosonic [BDZ08] and fermionic [Ess10, TSP18] Hubbard models using atoms trapped in optical lattices, and Ising models employing Rydberg atoms in optical tweezers [BBL16]. During the last years, ultracold atoms have also been proposed as appropriate candidates to engineer gauge theories, expanding the scope of quantum simulation from low to high energy physics [BC20]. In addition, Rydberg atoms have consolidated as one of the most promising implementations of digital gate-based quantum computing [HBS+20].

Although traditionally alkali metals like potassium and rubidium had been the preferred choice for cold atoms experiments due to their relatively simple single-valence-electron structure, other elements with two valence electrons have gained relevance in recent years. In particular, in one of the teams of the ultracold quantum gases group at the Institute of Photonic Sciences (ICFO) we are working with *strontium*. Unlike alkali metals, strontium features a stable fermionic isotope (^{87}Sr) with nuclear spin $I = 9/2$, in addition to three bosonic isotopes, as well as optical transitions convenient for laser cooling, trapping and Rydberg-state preparation [SPGS13, DKYB16].

The experimental apparatus, that is in the last building stages, has already shown cooling to few nK and it will soon be equipped with an optical lattice and a quantum gas microscope that will provide single-site spin-resolved imaging. On the one hand, the spin characteristics of ^{87}Sr will be used to extend the work done, for instance, in [TYST12] and explore the vastly rich dynamics of multicomponent Fermi-Hubbard models [NM14], which includes metallic and insulating phases, exotic magnetic order and superconductivity. On the other hand, the scattering properties of ^{84}Sr, which allow the use evaporative cooling to Bose-Einstein condensation, and the absence of hyperfine structure, that enables the realization of an almost ideal two-level system, make it ideal for studying collective coherent effects in atomic arrays [AGMCA+17, SWLY17, RWRA+20], such as sub-, super-, and selective radiance. Another experiment involving Rydberg strontium atoms with the goal of simulating Ising models and lattice gauge theories will start in the group in September.

Preparing an atomic system in such intricate states is nothing but challenging. It requires a high level of control as atoms undergo the different laser cooling and trapping stages from the source to the science chamber. The outcome of this technically demanding

process, however, is limited by the *atomic source* itself. Understanding the behaviour of the atomic beam that comes out the source and optimizing it would result in a higher number of atoms at the beginning of the journey, which would translate into a higher number of atoms in all the subsequent cooling stages. In our case, where the natural abundance of the isotopes we want to work with is low, this is crucial to reach the regime of quantum degeneracy needed to conduct the desired quantum simulations.

With this motivation, during this thesis we have built an atomic source of strontium and a setup designed for the characterization of the atomic beam with spectroscopy techniques and its optimization via laser cooling. We have structured the description of this process in the following way. Section 2 lays the theoretical foundations regarding strontium source, spectroscopy and cooling. In Section 3 we detail the experimental setup used, which includes a vacuum system and an optical setup. Section 4 showcases the different spectroscopy measurements taken and the relevant information extracted of them, as well as a proof of transverse laser-cooling enhancement.

2 Theoretical background

This section collects the theoretical considerations that we deem to be essential for the understanding of our work. First, we provide and introductory background for the laser spectroscopic and cooling techniques used. Then we offer an overview of the strontium nuclear and electronic structure, highlighting relevant features for atomic physics experiments. Finally, we discuss the main ideas behind the design of our atomic source.

2.1 Spectroscopy

When considering atom-light interactions, the probability that a photon of a given angular frequency ω is absorbed exciting the atom to a certain excited state has a Lorentzian shape centered at the corresponding transition frequency ω [Foo07]:

$$g(\omega) = \frac{1}{\pi} \frac{\gamma}{(\omega - \omega_0)^2 + \gamma^2} \tag{1}$$

The full width at half maximum (FWHM) $\Gamma = 2\gamma$ is called *natural transition linewidth*. Due to Heisenberg uncertainty principle, regarding Γ as an uncertainty in the energies of the states, it also characterizes the typical time after which the atom will decay to a lower energy state, being inverse proportional to it. In this spontaneous decay process, a photon is emitted in a random direction with frequency again distributed according to the Lorentzian shape of the transition. The emission is not isotropic, following a dipole emission pattern: a toroidal distribution with the axis determined by the light polarization.

We consider a beam of monochromatic light of intensity I interacting with a stationary cold atomic cloud of atomic three-dimensional density $\rho(y)$, which we assume that only has dependence in the direction of the beam y. For simplicity, we will consider the light frequency close to resonance with a single transition between two states that we will suppose that form a perfect two-level system. The interaction will yield an attenuation in the intensity of the beam, as some photons are absorbed and the re-emitted photons may not have the same direction. A small slab of thickness Δy will contain $\rho(y)\Delta y$ atoms per unit area which will absorb a photon with probability $\rho(y)\sigma(\omega)\Delta y$, where $\sigma(\omega)$ is the atom-photon cross-section, which at resonance is $\sigma(\omega_0) = 3\lambda^2/2\pi$ [Foo07]. Equaling this probability to the fraction of intensity loss $\Delta I/I$, we obtain the *Beer-Lambert law*:

$$\frac{dI}{dy} = -\rho(y)\sigma(\omega)I \Longrightarrow I(y,\omega) = I_0 e^{-\sigma(\omega)\int_{y_0}^{y}\rho(\tilde{y})d\tilde{y}} = I_0 e^{-\sigma(\omega)n} \tag{2}$$

where n is the column integrated density: the total number of atoms encountered by the beam per unit of transverse section area from y_0 to y. The intensity outcome as a function of the frequency yields an *absorption signal* that will reflect the Lorentzian absorption shape and will be proportional to the atomic population that light encounters. On the other hand, the photons that are emitted in different directions can be detected when looking at the intersection of the beam path with the atomic cloud from one of these direction. This emission phenomenon is called *fluorescence*. Although fluorescence is typically not useful to quantify the absolute absorption value, since we only see a fraction of the emitted photons, it offers the spatial resolution that an absorption signal lacks, as its intensity at each point of the beam path can be resolved. This is useful to estimate atomic density profiles.

If the atoms are moving with non-relativistic velocity $\vec{v}$ with respect to a light source that produces photons with wavevector $\vec{k}$, the relative radial velocity in the direction of the light propagation is given by $v = \vec{v} \cdot \vec{k}/|\vec{k}|$, taken positive if the atoms move away from the source. Then, the frequency perceived by the atoms, ω', will be shifted with respect to frequency of the emitted light, ω, according to the Doppler effect by

$$\omega' = (1 - \frac{v}{c})\omega \Longrightarrow \Delta\omega = -\frac{v}{c}\omega = -\frac{\omega\lambda}{2\pi c}\vec{v} \cdot \vec{k} = -\vec{v} \cdot \vec{k} \tag{3}$$

where c is the speed of light and λ the emitted wavelength. Consequently, if the atoms move towards the source they will observe a higher frequency, shifting therefore the absorption shape towards lower frequencies, and the other way around. This is known as *Doppler shift*. If many velocities are present in the atomic cloud, for instance due to a thermal distribution, the probability that frequencies away from the natural transition frequency are absorbed increases, resulting in a broadening of the natural absorption shape known as *Doppler broadening*. These two effects are used in spectroscopy to obtain information about the atomic velocity distribution.

2.2 Doppler cooling

During the interaction with the light beam, in an absorption event, the photon will transfer its momentum $\hbar\vec{k}$ to the atom. Conversely, during emission, the atom will recoil in the opposite direction of the emitted photon. However, whereas all the absorbed photons move in the same direction, the recoil caused by an emitted photon is in a random direction, and as the emission is equiprobable in opposite directions, it averages to zero after many events. This results in a net momentum transfer from the light beam to the atoms. The associated force is called *radiation pressure force* and is modeled by [MvdS99]

$$\vec{F} = \frac{\hbar\Gamma s_0}{2} \frac{1}{1 + s_0 + 4\left(\frac{\delta - \vec{v}\vec{k}}{\Gamma}\right)^2} \vec{k} \tag{4}$$

where $\delta = \omega - \omega_0$ is the detuning of the light frequency ω with respect to the transition frequency ω_0 and $s_0 = I/I_0$ with $I_0 \simeq \omega_0^3\Gamma$ being the saturation intensity. The term $\delta_{\text{total}} = \delta - \vec{v} \cdot \vec{k}$ is the effective detuning obtained when taking into account the Doppler effect, and introduces a velocity dependence in the force.

Considering now two counter propagating beams with the same intensity I and opposite wavevectors $\pm\vec{k}$, the net force will be given by

$$\vec{F} = \vec{F}_{\vec{k}} + \vec{F}_{-\vec{k}} = \frac{\hbar\Gamma s_0}{2} \left(\frac{1}{1 + s_0 + 4\left(\frac{\delta - \vec{v}\vec{k}}{\Gamma}\right)^2} - \frac{1}{1 + s_0 + 4\left(\frac{\delta + \vec{v}\vec{k}}{\Gamma}\right)^2} \right) \vec{k} \tag{5}$$

For red detuned light ($\delta < 0$), the behaviour of this force as a function of the atomic velocity projection v (Fig. 1) exhibits a region with negative slope that crosses zero, indicating a viscous damping. This means that the atoms with velocities in this domain will be slowed down or, thinking from a thermal perspective, cooled down, in the direction of the beam while interacting with it. Intuitively, each counter propagating red detuned beam will interact with the atoms that move towards the photon sources, exerting a force in the opposite direction. This effect is called *Doppler cooling* and is the foundation for many laser cooling and trapping techniques. For velocities outside this region there is also cooling but less efficient. Blue detuned light has the opposite effect, heating up the atoms.

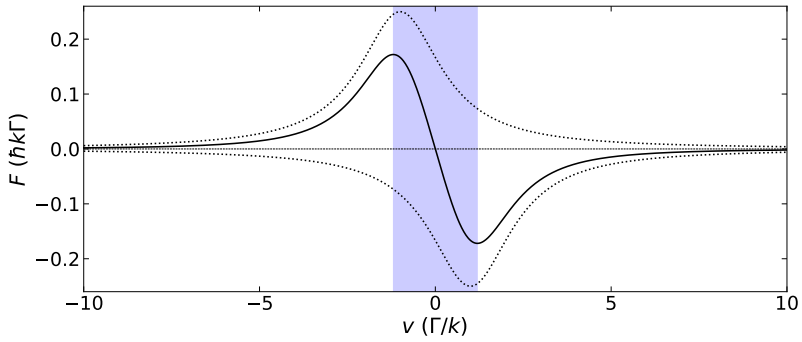

Figure 1: Module of the force F in Eq. 5 for $s_0 = 1$ and $\delta = -\Gamma$. The dotted lines correspond to the force exerted by each beam and the shaded area highlights the cooling region as such.

The larger Γ is, the wider the velocity range of the cooling region will be. However, the random-walk-like process caused by the constant absorption-emission events limits the temperature the atoms can be cooled down to. This temperature is called *Doppler temperature* and is proportional to Γ according to $T_{\text{Doppler}} = \hbar\Gamma/2k_B$ [Foo07]. Therefore, there is a trade-off between the range of velocities and the minimum temperature to which the cloud can be cooled down.

2.3 Properties of strontium

Strontium is the element of atomic number 38. There are 4 stable isotopes: ^{88}Sr (with natural abundance of 82.58%) , ^{87}Sr (7.00%), ^{86}Sr (9.86%), ^{84}Sr (0.56%) [Ste13]. Since the number of protons is even, the isotopes with an even mass number have also an even number of neutrons, resulting in the nuclei arranging in pairs of anti-parallel spins giving raise to total nuclear angular momentum or nuclear spin null. This confers these isotopes a bosonic character. In ^{87}Sr the level that the unpaired nucleon occupies in the nuclear shell model entails a nuclear spin of $I = 9/2$, making it a fermionic isotope [Ste13].

As all alkaline earth metals, Sr has two valence electrons filling up the outer s-shell in the ground state. This results in a zero total spin ground state with these electrons anti-parallel aligned. Excited and doubly excited states can either be singlet $S = 0$ or triplet $S = 1$. A partial energy level diagram and some relevant transitions for cooling and trapping strontium are represented in Fig. 2 [Ste13].

The transition we have worked with in this thesis is the broad *blue transition*, with $\Gamma = 30.5 \cdot 2\pi$ MHz, which connects the ground state $5s^2\ {}^1S_0$ with the $5s5p\ {}^1P_1$ singlet state at 460.862 nm. In strontium, the spin-orbit interaction is large enough, to marginally overcome the selection rule $\Delta S = 0$ that forbids spin-flip transitions in small Z elements. An example of this is the narrower *intercombination red transition*, with $\Gamma = 7.4 \cdot 2\pi$ kHz,

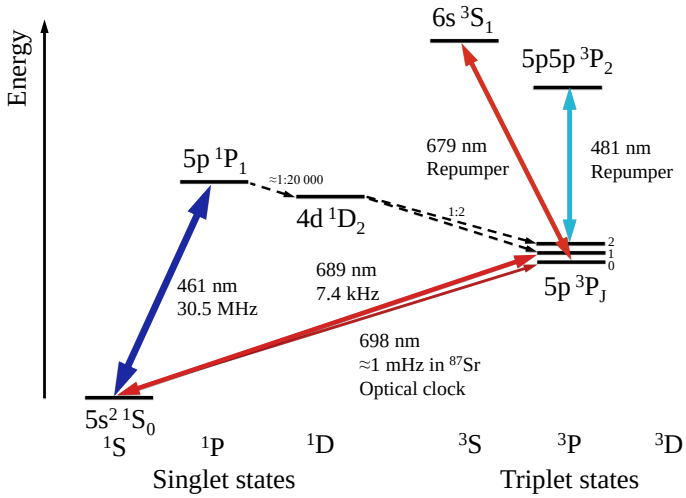

Figure 2: Sr energy levels. We use the usual spectroscopy notation $nlnl^{2S+1}L_J$ where n and l denote respectively the principal number and the orbital angular momentum number of each of the valence electrons, and S, L, J are the total spin, total orbital angular momentum and total angular momentum of the atom. For single electron excitations the first $5s$ is omitted. The wavelengths and the linewidths $(\Gamma/2\pi)$ of some transitions are also shown as well as some decay channel ratios.

connecting $5s^2\ ^1S_0$ and $5s5p\ ^3P_1$ at 689.449 nm. The only decay channel of this excited state is directly back to the ground state, forming a perfect two-level system (except for ^{87}Sr, where the hyperfine structure due to the nuclear spin splits this level into three). These two transitions play a central role in the laser cooling and trapping of strontium, as they linewidths complement each other to capture a broader range of velocities and cool further down respectively. The Doppler temperatures are $T_{\text{Doppler}} = 720\ \mu$K for the blue transition and $T_{\text{Doppler}} = 179$ nK for the red.

Due tot the difference in mass and size of the nucleus of the different isotopes, they exhibit slightly different transition energies, what is known as *isotopic shifts*. For instance, for the blue transition, these shifts are with respect to the ^{88}Sr value of -46.5 MHz, -124.8 MHz, -270.8 MHz for ^{87}Sr, ^{86}Sr and ^{84}Sr respectively [Ste13].

The *clock transition*, between $5s^2\ ^1S_0$ and $5s5p\ ^3P_0$, is also prominent. This transition, doubly forbidden by selection rules, can be addressed in ^{87}Sr thanks to the hyperfine structure given by the nuclear spin. Its extremely narrow linewidth of 1 mHz is useful in metrology to produce exceptionally precise optical clocks, where the transition frequency is used as a reference for timekeeping [KTPO03, LBY+15]. Due to its long lifetime (100 s for ^{87}Sr), the clock state can also act as an effective ground state from which Rydberg states can be prepared with a single relatively low-energy photon [DKYB16].

Finally, we have also highlighted two further transitions we use as *repumpers* in the cooling process. The atoms that decay through alternative channels to long-lived excited states cannot be excited again with the blue transition for some period of time, resulting in a loss of cooling efficiency. Re-exciting them with these transitions, causes them to rapidly decay back to the ground state, reintroducing them into the cooling cycle.

2.4 Atomic source

Strontium is solid at room temperature, so to obtain an atomic cloud, we first have to evaporate it. An *atomic oven* is a solution to produce vapour by simply heating up the strontium. Despite its melting point is at 770°C, quite large compared to other elements as

potassium or rubidium, at temperatures above 400°C the amount of vapour that co-exist with the solid starts being sufficiently large. Typical working temperatures range from 450°C to 600°C [SRG+15, Sta19, Cas20]. In this regime, the strontium gas can be modeled as an ideal gas, displaying a Maxwell-Boltzmann velocity distribution for which the most probable velocity is $v_p = \sqrt{2k_BT/m}$ with m being the atomic mass.

In order to capture as many atoms as possible in the first trapping section, which will have a limited range of action, it is convenient to produce a high-flux collimated atomic beam directed towards it. The simplest atomic oven architecture that serves this purpose consists of a reservoir with an aperture. Without limiting this aperture, the strontium vapour would expand in all directions, meaning that only a small fraction of atoms would reach the first trapping section. The remaining atoms would be lost, contaminating the vacuum and quickly emptying the strontium reserves increasing the amount strontium refills needed, a particularly delicate process which involves opening the vacuum system. For an effusive beam, the most probable velocity has to be corrected with a factor of $\sqrt{3/2}$ to account for the fact that faster atoms are more likely to pass through the aperture [Foo07]. For 450°C and 600°C this corresponds to 452.999 m/s and 497.769 m/s respectively.

The characteristics of the outgoing atomic beam depend on the properties of the aperture, namely its diameter d, its length L and the ratio $\beta = d/L$ between them. The atoms that have high transverse velocities with respect to the aperture axis will collide with its walls, slowly or not even exiting the oven. Therefore, the smaller the ratio β is, the less transverse velocities will contribute to the atomic beam, i.e., the less divergent it will be (Fig. 3). However, the outgoing flux is proportional to the section of the aperture. For this reason, the single hole aperture is often replaced by a nozzle with an array of *microcapillaries*, long thin tubes with small β, stacked together to keep the flux high by adding up all their contributions [SPP+12, SRG+15].

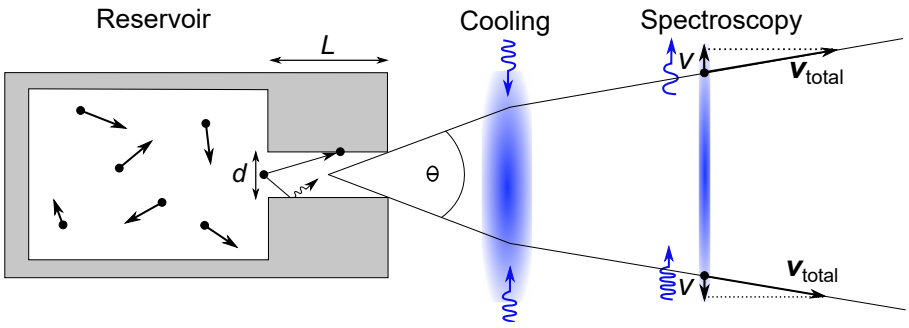

Figure 3: Representation of the atomic beam emerging of an oven and the principles behind Doppler spectroscopy and cooling. The relevant aperture parameters and the divergence angle are highlighted.

With the spectroscopy techniques we have described in Section 2.1 it is possible to obtain the velocity and density distributions of the atomic beam. Given its inherent divergence, we expect to observe that the closer the atoms are to the laser source side of the oven, the more red detuned the light they are in resonance with will be, and equivalently for the opposite side and blue detuned light (see Fig. 3). The density is expected to be higher in the region around the axis of the beam, where the microcapillaries direct most the flux, and rapidly decrease as we overcome the divergence angle θ.

This atomic source can be completed by adding to the atomic oven a *transverse cooling* stage. In its most simple version, one-dimensional transverse cooling, it is realized by two counter propagating red-detuned laser beams in the transverse direction of the atomic beam. As explained in Section 2.2, this configuration slows down the atoms in this direction, collimating the atomic beam and increasing its brightness at the experiment position.

3 Experimental setup

Cold-atom experiments are carried out in high or ultra-high vacuum environments. This is crucial to extend the lifetime of the cooled-down systems by minimizing the collisions with the residual background gas, which is not affected by the cooling process. To test the atomic source in its operating conditions we must therefore set up a vacuum system, attaching the oven to a rigid enclosure where the residual gas is pumped out: a vacuum chamber.

The other essential ingredient for spectroscopy will be light quasi-resonant with a strontium ground state transition. In our case, we have chosen to work with the blue transition, which is easier to address for being broader, and therefore has also a wider range of capture velocities when cooling, a range that matches the order of the transverse velocity of the atomic beam. Hence, an optical setup based around a 461 nm laser system, is also needed.

In this section we will describe all of these elements that constitute our experimental setup.

3.1 Vacuum system

The vacuum level one can reach is usually limited by the so-called *outgassing*. This process consists of a gas release by substances that had been adsorbed onto the interior surfaces of the vacuum chamber or even trapped in the bulk of the metal vacuum components. Typically, this gas release rate is much larger than the rate of gas slowly leaking through micro apertures in the junctions between pieces. To maintain the vacuum pressure, therefore, one has to remove these outgassed molecules by constantly pumping. In our case, we use a pump [1] that combines a initial stage of roughing pumping, which removes the atmospheric air, mostly H_2 and N_2, up to 10^{-3} mbar, and a steady stage of turbomolecular pumping, which can reach pressures around 10^{-10} mbar. This pump is connected to the main chamber through a valve (Fig. 4 (11)) using a bellow, and powered through an uninterrupted power supply (UPS). Below 10^{-5} mbar, the balance between the pumping rate and the outgassing rate will determine the final pressure level.

Some sources of outgassing can come from the fabrication of the vacuum components, so it is necessary to clean the interior surfaces with volatile chemicals. Furthermore, even the bare contact with the atmosphere will cause the absorption of molecules that will outgas, mainly water, carbon dioxide and hydrogen. In order to minimize this, it is critical to use low-outgassing materials [MCD83], such as stainless steel, with surfaces polished to remove the impurities that increase the absorption of molecules. In our case, all the components are made of 316LN stainless steel. In addition, outgassing can be further reduced after a *baking* or *bake-out* process. This technique consists in heating up the entire vacuum system while pumping it to drastically accelerate the outgassing and remove most of its source. This allows to reach a lower final pressure once the chamber has been cooled down, being typically hydrogen the only remaining outgassing source.

The two main parts of our vacuum system, the *spectroscopy chamber* and the *atomic oven*, that had been prepared following different assembly and bake-out procedures. Next, we provide, together with the concept behind their design, a summary of this process. The technical details regarding the vacuum preparation can be found in Appendix A.

[1] Pfeiffer Vacuum HiCube

3.1.1 Spectroscopy chamber

The spectroscopy chamber is composed of several pieces[2]. All these pieces feature ConFlat (CF) flanges for the junctions between them, which are sealed with non-reusable copper and nickle gaskets, in which the circular knife edge of each flange cuts in. In order to characterize the atomic beam using spectroscopy, the interior of our vacuum chamber must be optically accessible. This is achieved by installing glass windows known as *viewports*. With the focus on having an extensive optical access to maximize the number of positions and angles at which we can interact with the atomic beam, we have opted for a design, depicted in Fig. 4, that features a pair of large CF63 (63 mm of nominal diameter (ND)) viewports[3] (7). Moreover, using a zero-length adapter (3) from the oven (1),(2) to the main cube (4), these viewports are set as close as possible to the oven in the longitudinal direction. This enables the study of the beam behaviour right after the nozzle, and also the implementation of a more effective transverse cooling. Nevertheless, the viewports are connected to the cube with 70 mm adapters (6), that provide some distance in the transverse direction with respect to the atomic beam and prevent the glass from strontium coating, which would make it opaque. Smaller CF40 viewports[4] (8) are placed in the vertical axis to offer the possibility of imaging the fluorescence inside the chamber.

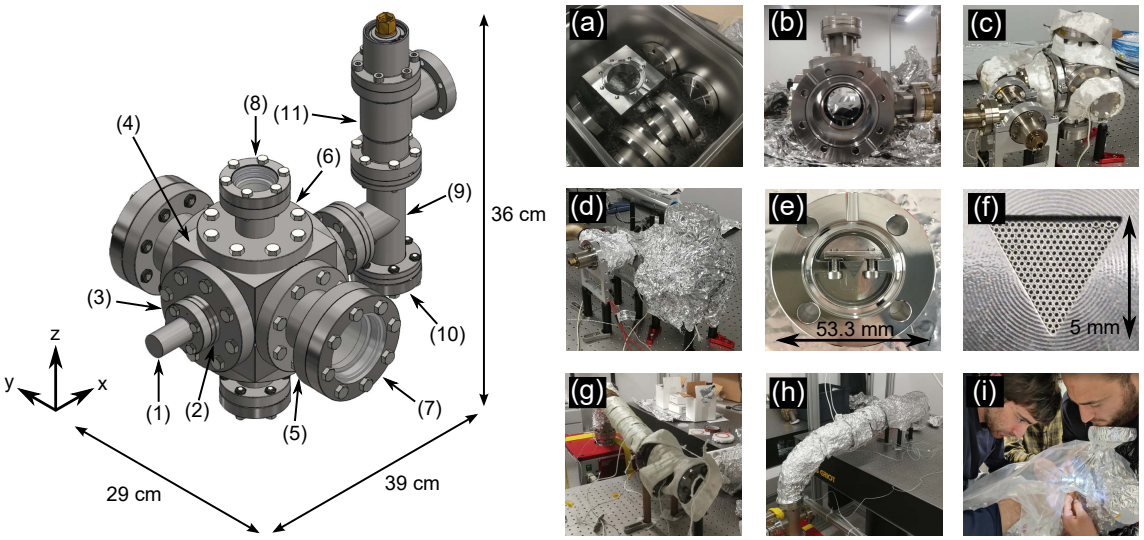

Figure 4: Left. CAD render of the vacuum system: (1) reservoir, (2) nozzle, (3) CF25/63 zero-length adapter, (4) CF63 cube, (5) CF63/63 70mm adapter, (6) CF63/40 70 mm adapter, (7) CF63 viewport, (8) CF40 viewport, (9) CF40 T, (10) CF40 blank, (11) Valve. Right. Preparation of of the vacuum system: (a) Ultrasonic bath, (b) chamber assembly, (c) chamber baking preparation, (d) chamber baking, (e) nozzle flange, (f) detail of the microcapillaries array, (g) oven baking preparation, (h) oven baking, (i) strontium loading.

All the chamber pieces were cleaned using an ultrasonic bath (Fig. 4 (a)) of acetone and ethanol, and assembled taking the necessary precautions to avoid contaminating them. Two successive bake-outs were carried out: a first high-temperature 400°C bake-out with blank flanges replacing the viewports, and a gentler 190°C second bake-out with the viewports installed (see Appendix A). In this way we can subject the main chamber pieces to a more effective aggressive bake-out without damaging the viewports. The bake-outs were executed by wrapping the whole chamber and bellow with resisitive fiber glass heating tapes (Fig. 4 (c)) and isolating them with numerous layers of aluminum foil (Fig. 4 (d)) to

[2] Pieces made by VACOM [3] VACOM VPCF40B-L [4] VACOM VPCF63B-L

increase the heating efficiency. The temperature and pressure were monitored in real time using various thermocouples adhered to selected key points on the system and a pressure gauge installed in the turbopump respectively. With this process we reached a pressure of $2.9 \cdot 10^{-9}$ mbar.

3.1.2 Atomic oven

Our oven concept follows the design of D. Weld group [SRG+15]. The reservoir consist of a cylinder of 21 mm of inner diameter and 45 mm of length welded onto a CF25 flange in one side and closed in the other. The nozzle is formed by an hexagonal microcapillary array clamped to a CF25 flange (Fig. 4 (e),(f)). This geometry is chosen to minimize the gap between microcapillaries, which could potentially ruin the collimation, and is guaranteed by using an equilateral triangle-shape aperture, which is cut by electrical discharge machining to ensure defects sufficiently smaller compared to the microcapillaries size. The microcapillaries [5] are made of 304 stainless steel and feature a outter nominal diameter of 321.42 μm, a nominal inner diameter of 210.82 μm and a length of 10.67 mm.

Apart from acetone and ethanol, we also used soap to clean the microcapillaries, before being manually insterted and clamped in the nozzle. The bake-out of the assembled nozzle and the reservoir was carried out in parallel to the chamber bake-out. The reason is that we wanted to reach a higher temperature (namely 700°C) than their typical working temperature to ensure that their outgassing is low. We placed them inside a CF63 T (Fig. 4 (g), (h)) that was connected to a second turbopump. After the bake-out, the pressure in the T improved from the initial $4.53 \cdot 10^{-8}$ mbar to around $1 \cdot 10^{-10}$ mbar (Appendix A).

The strontium[6] loading and the oven installation were carried out in a glovebox filled with argon (Fig. 4 (i)). This is essential, not only to avoid the atmospheric contact with the baked-out pieces, but also with the strontium itself, which rapidly oxidizes. We placed a heating band [7] around the nozzle flange to keep the nozzle hotter and avoid clogging of the microcapillaries. We added a layer of micropourus blanked isolation, followed by several layers of aluminum foil. We started cycling the temperature between 400°C and 600°C in the nozzle when the experiment was in standby and running respectively to save strontium. However, due to the proximity of the oven with the chamber, the temperature gradient during this cycle opened up a leak in the junction. After cooling down and re-tightening the screws to fix the leak, we decided to keep the temperature constant at 508°C. The pressure we read at this temperature is around $1.5 \cdot 10^{-8}$ mbar.

3.2 Optical setup

Our optical setup consists of five distinct parts. First we have the laser system, which produces narrow-linewidth coherent light quasi-resonant with the blue transition. This light is then send through optical fibers to the second stage, the measurement setup, which directs the beams in different configurations towards the chamber, where they interact with the atomic beam, and collects afterwards the absorption signal. Since most of the decays from the $5s5p\ ^1P_1$ state lead back to the ground state, for our purposes we can consider that light is effectively interacting with two-level atoms. Two more parts are a grating wavemeter and a Fabry-Perot cavity, that are used to calibrate the laser frequencies. The setup is completed with a CCD camera imaging system to get the fluorescence data.

[5] MicroGroup 304 SS WD 0.0123" OD X 0.0083" ID x 0.420" +/- 0.010" CUT LENGHTS DEBURR [6] Sigma-Aldrich 441899-5G strontium, dendritic pieces, 99.99% [7] Watlow MI Band Heater Ref. MB2A1JN1-B12, 400 W, 8.2 W/cm2

3.2.1 Laser system

For our spectroscopy purposes, we need narrow-linewidth lasers with a smoothly fine-tunable frequency over a sufficiently wide range. These requirements are met by grating-stabilized *external cavity diode lasers* (*ECDL*) (see Appendix B for an overview), where a grating is used to select and smoothly tune one of the cavity modes the laser emits in. Implementing and characterizing the transverse cooling effect using spectroscopy requires to control the frequency of two beams independently, one for cooling and the other for probing. Although this can be achieved using a single laser and acousto-optical modulators, which shift the frequency of the beam, we have opted for using two independent master lasers. The main laser, that we use for taking all the characterization measurements and for cooling, is a commercial ECDL with a low-power master output and a high-power slave output[8]. It produces around 100 mW before the fiber in the master output, but it can reach 800 mW when amplified via *injection lock* with the integrated slave diode. This technique forces a high-power broad laser diode (slave) to emit single mode at the frequency of a low-power narrow laser (master) the light of which is injected in the slave, provided that the frequencies are close enough. An electronic controller allows to adjust the current and the temperature of the diode and drive small grating angle adjustments thanks to a piezo-electric actuator. It is also possible to automatically scan the frequency of the laser by modulating the voltage in the piezo-electric actuator with a periodic signal. In our case we generate a triangular symmetric signal of the desired frequency with an external signal generator, and we set the amplitude of the scan with the controller.

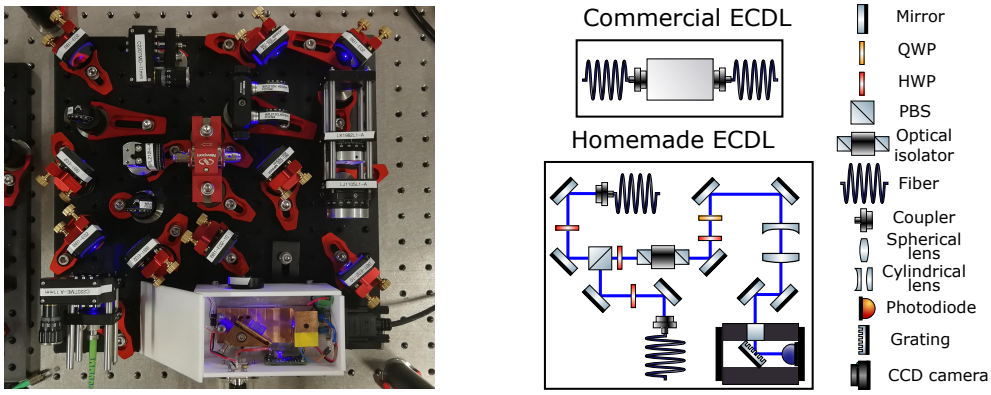

Figure 5: Diagram of the laser system together with a picture of the homemade ECDL setup.

The second laser, used for probing the atomic beam under cooling, is a homemade ECDL. The diode[9], the collimator lens [10], the grating [11] and the piezo-electric actuator [12] had already been assembled following a Littrow configuration in a custom-made mount isolated with a teflon box (see [Est21] for the design). Once we alligned the grating such that there was lasing around 461 nm, we built a setup for the refinement of the beam. The elliptical beam profile is corrected with a cylindrical lenses [13] [14] telescope and stabilized with an optical isolator [15] that prevents undesired external feedback (see Fig. 5). To match the optimal polarization input in the isolator, a quarter-waveplate [16] (QWP), to obtain linear polarized light from elliptical, and half-waveplate[17] (HWP), to rotate the axis of linear polarized light, are used. Then the light is coupled to two fibers, with the

[8] MOGLabs 461nm high power laser system, >750mW after isolator [9] Nichia NDB4216 [10] Thorlabs LT110P [11] Thorlabs GH13-36V (3600 grooves per mm) [12] Piezomechanik PSt150/4/5 [13] Thorlabs LJ1105L1-A [14] Thorlabs LK1982L1-A [15] Newport ISO-04-461-MP [16] FOCtek WPL212Q 460.9 [17] FOCtek WPL212H 460.9

power splitting being set by the orientation of the HWP preceding the polarizing beam splitter (PBS) [18], which reflects vertically polarized light and transmits the horizontal component. Current, temperature and piezo-electric actuator voltage are controlled with driver controllers[19].

3.2.2 Measurement setup

The main setup consist of two breadboards, one in each side of the chamber, elevated with respect to the optical table so that the beam height matches the center of the CF63 viewports. There are two different optical paths, both of which start with an outcoupler[20] and two PBSs, the first one for polarization cleaning and the second one for regulating the power. In the cooling configuration (Fig. 6), a probing beam is send through the chamber, with linear polarization given by the orientation of a HWP, and collected in the other side by a photodiode[21] connected to an oscilloscope. In this way we can measure the absorption signal. To create two counter propagating cooling beams, in the second path path the beam diameter is increased by a telescope, to widen the region where it interacts with the atomic beam, and retroreflected on the other side of the chamber. Interference between them is avoided by using two QWP so that the incident and reflected beam have opposite circular polarization. After the last QWP the reflected beam has a polarization perpendicular to the incoming beam so it is transmitted and filtered out by the second PBS instead of being reflected back to the outcoupler. This configuration can be adapted

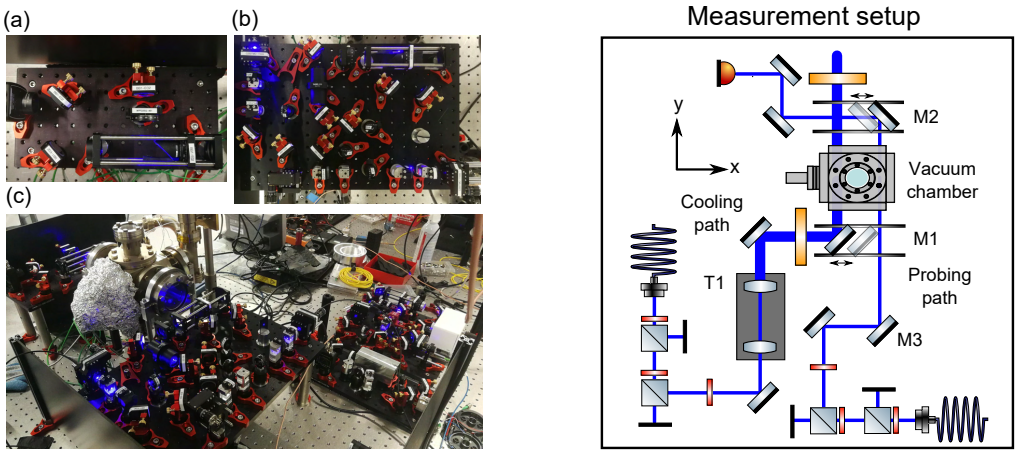

Figure 6: Diagram of the measurement setup together with pictures of the two breadbords, (a) and (b), and and overall shot of the experimental setup, (c).

to perform the other characterization measurements (cf Fig. 8). The mirror M3 can be realigned to send a beam with an angle, while removing the telescope T1 and blocking the back reflection transforms the cooling beam into another probing beam. The mirrors M2 and M3 are mounted in a cage system that enables a translational degree of freedom so that the beam can be easily send and collected in different positions along the viewport.

3.2.3 Calibration and imaging tools

In order to set the laser frequency in resonance with the atomic transition we rely on observing fluorescence inside the chamber. This is accomplished with a charge-coupled device (CCD) camera [22] connected to the computer. A software allows us to monitor in

[18] FOCtek PBS5204 (H-ZF2) 450∼680 [19] Toptica Sys DC 110 [20] Lens: Thorlabs C220TME-A
[21] Thorlabs DET10A2 [22] Point Grey CMLN-13S2M-CS

real time the interior of the chamber until we observe fluorescence, and, subsequently, take fluorescence data using a Python script which can save snapshots at different moments in time. The image is obtained using a 45° tilted 2" mirror below the bottom CF40 viewport and a system of two lenses that demagnify it and focus it on the camera so that we can see the whole top CF40 viewport from the bottom. A band-pass optical filter is used to reduce the ambient light.

However, before obtaining fluorescence we first need to tune the laser so that it emits single-mode and close enough to resonance for small current and piezo-electric actuator adjustments to reach it. For this purpose we use an already built *grating wavemeter* [Est21]. It operates with a lens that collimates the light that comes out of a fiber onto a grating. The diffracted beams, the direction of which is wavelength dependent, are focused onto another CCD camera so that each wavelength present in the light appears as vertical line on the screen. In this way, we can observe when the laser is emitting in a single or multiple modes. In addition, we can measure the position on the screen of the line produced by a laser that we know is operating in resonance, to have a rough reference of where the resonance is. For this calibration, we use resonant light from another laboratory.

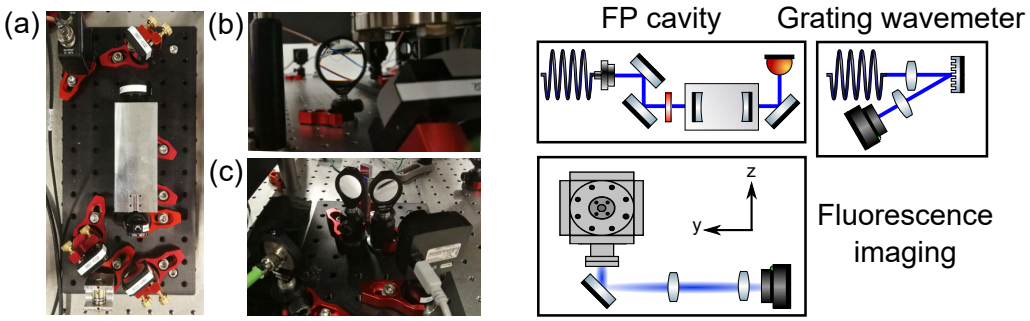

Figure 7: Diagram of the optical calibration tools together with pictures of (a) FP cavity, (b) grating wavemeter, (c) fluorescence imaging setup.

Although from fluorescence and absorption we can identify the resonance frequency, during a frequency scan the only information we can in principle obtain is the piezo-electric actuator voltage, which is not enough for finding which frequency corresponds to each scan point. For this reason we built a confocal *Fabry-Perot cavity*, using a custom-made aluminum cavity closed by two plano-concave mirrors[23] placed in adjustable mounts. They are set such that their radius (10 mm) matches the length of the cavity. Sending the light through the cavity while scanning the laser piezo-electric actuator voltage and collecting it at the output with a photodiode will produce a peak in the oscilloscope every time the frequency matches a cavity mode. The separation in frequency of two consecutive modes is called free spectral range (FSR) and only depends on the known length of the cavity by $\mathrm{FSR} = c/4L$. Therefore, measuring in the oscilloscope the piezo-electric actuator voltage drop between two cavity peaks, and assuming a linear dependence we can map voltage (and knowing the scan period, time) to frequency relative to the resonance.

Additionally, the isotopic shifts are also useful to calibrate the voltage-frequency relation. The main peak or dip in a fluorescence or absorption signal corresponds always to the resonance of ^{88}Sr which is the dominant isotope. However, in some circumstances, it is also possible to spot a secondary bump which corresponds to ^{86}Sr, the second most abundant isotope (see Fig. 9 (c)). Once confirmed that the frequency distance between the two peaks is compatible with their isotopic shift with a first cavity calibration, we can use the known value of the shift as a more precise calibration.

[23] Layertec Output Coupler 130383

4 Measurement results

With the experimental setup we have described, we have performed different spectroscopic measurements on the atomic beam. These can be grouped in three categories. First, we carried out transverse measurements, where a laser beam was sent perpendicular to the atomic beam axis at different positions (Fig. 8 (a)). The resulting fluorescence data allow us to reconstruct a two-dimensional transverse velocity and density profiles, whereas the absorption data is useful to quantify the atomic density. Then, we estimated the longitudinal velocity of the atoms in the axis of the beam by measuring the Doppler shift in fluorescence of two beams, one sent transversely and the other with an angle (Fig. 8 (b)). Finally, the last set of measurements were targeted at evaluate the transverse cooling effect with the absorption signal of a probe beam (Fig. 8 (c)).

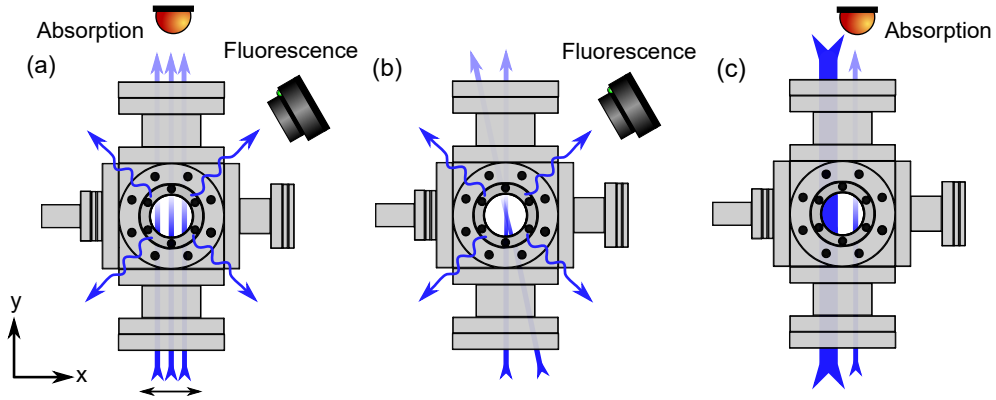

Figure 8: Schematic representation of the different measurements performed. (a) Transverse measurements, (b) longitudinal measurements, (c) transverse cooling measurements.

4.1 Transverse measurements

With transverse measurements we want to estimate the transverse velocity and density distribution in y at different distances x from the oven. The first of these goals is accomplished using fluorescence and the Doppler effect, as the frequency at which a certain point will exhibit a maximum in fluorescence will reveal its velocity in the laser beam direction. Therefore, to obtain this information for the position x we want to probe, we just need the fluorescence intensity of each point along the y axis as a function of the detuning.

Additionally, the amplitude of the fluorescence maximum will be proportional to atomic density at each point, disclosing the shape of the density profile. However, since with fluorescence is not possible to capture all the photons, to estimate quantitatively these density we need an absorption signal, which will provide an attenuation value that accounts for all the photons losses and is a function of the atoms per unit area that the beam encounters (Eq. 2).

Fluorescence and absorption signals are obtained with a frequency scan in the low-power master output of the commercial laser. We use a triangular signal modulation of amplitude manually determined by setting the laser barely off-resonance with any velocity class present in the atomic beam in the extremes of the ramp signal. Due to divergence of the beam (see Fig. 3) we see the fluorescence maximum moving from one extreme of the imaging range to the other between a maximum and a minimum of the modulation signal.

4.1.1 Fluorescence

Before taking fluorescence data, we first observe that the intensity of the fluorescence detected through the vertical CF40 viewports depends drastically on the orientation of the linear polarization we set, being almost zero for certain angles, but not if we observe it from the horizontal plane. We measured an intensity behaviour proportional to $\sin^2(\alpha)$, where α is the polarization angle respect to the vertical, which confirms that this effect is due to the dipole emission pattern of the atoms [SPP+12]. With this consideration, we drove the atoms with horizontally polarized light.

For a given distance x from the oven we set the laser power to 0.359 mW and saved fluorescence images over a frequency scan period. By processing this images (see Appendix C) we are able to obtain the sought fluorescence intensity signal of each y position at each detuning.

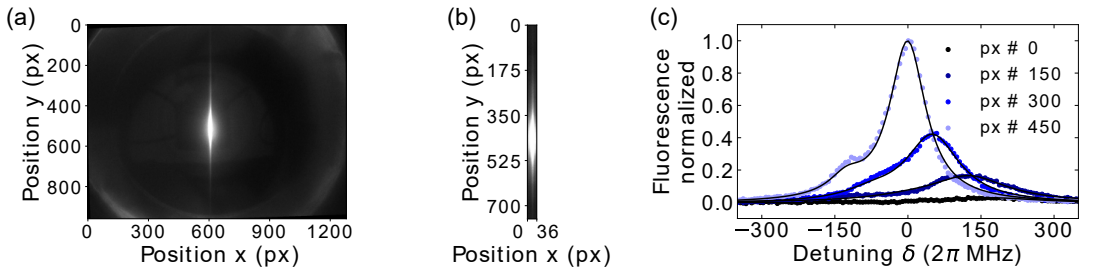

Figure 9: Fluorescence image processing from transverse measurements. (a) Example of a raw image saved. (b) Imaged cropped around the fluorescent region. (c) Fluorescence signal at different y positions as a function of the detuning at x=11 cm from the oven (more precisely the junction between nozzle and reservoir). Fits to a sum of two Lorentzian are also shown.

The results of some of these signals are shown in Fig. 9 (c). As we expected, we observe how as we move away from the axis of the atomic beam, the signal becomes less intense. In addition, we observe that the signal becomes broader. This can be explained by arguing that the spread in the transverse velocity, and therefore the Doppler broadening, should be proportional to its magnitude. The reason is that the spread in the module of the atomic velocities, given by the corrected Maxwell-Boltzmann distribution, is expected to be much larger than its angle spread within a small region. The higher the transverse velocity is, the larger will be the projection of the spread in the transverse direction.

Fitting these data to a sum of two Lorentzian, with the distance between peaks and the relative amplitudes fixed to account for the secondary isotopic bump, we can extract the relevant physical information of the beam. From the width 2γ we obtain the broadening of the signal, from the position of the peak, the trasnverse velocity, and from its amplitude, the density. In Fig. 10, we show an example of broadening, transverse velocity, and density profiles as function of the y position. We also show the density distribution in velocity. The profiles are centered fixing the zero detuning at the frequency where the y position with minimum broadening displays the maximum frequency. As previously discussed, in this position, the atoms are stationary in the transverse direction.

The broadening features the expected minimum in the center. The velocity behaviour is approximately linear, but exhibits a region with less slope around the center, which indicates that in this region the atoms are more collimated. Density profiles in space and velocity exhibit similar behaviours, being strongly distributed around the center position or velocity. The velocity density distribution is fitted to a Lorentzian from which we obtain a FWHM of 29.5 (0.2) m/s. The value of this parameter, which quantifies the beam divergence, increases as we measure closer to the oven. For instance, for $x = 7$ cm from

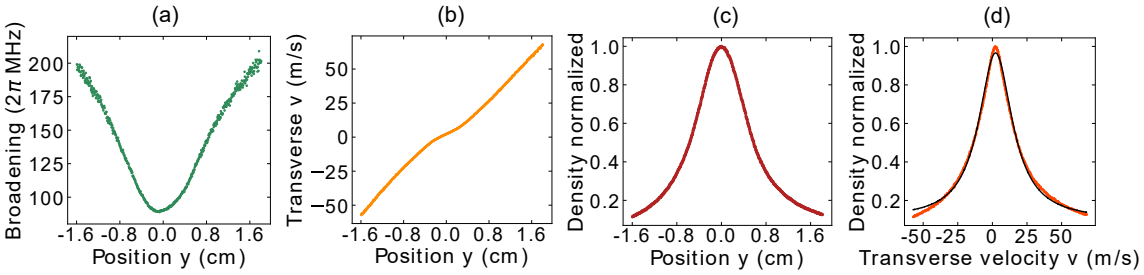

Figure 10: Transverse profiles at $x = 11$ cm from the oven. (a) Resonance broadening (FWHM) as a function of the position y. (b) Transverse velocity v a function of y. (c) Density normalized as a function of y. (d) Density normalized as a function of the transverse velocity v. For the last plot, a Lorentzian fit is included (FWHM=29.5 m/s).

the atomic beam the obtained FWHM is of 57.3 (0.4) m/s, almost twice. Since close to the oven the velocity range we interact with is larger, this value is more representative of the real divergence of the beam. It is approximately twice the value found, for instance, in [SPP+12], but the oven designs are not comparable as they used a second aperture.

Repeating the process for different x positions yield the different two-dimensional colormaps showcased in Fig. 11. We see how as we move away from the oven, the broadening and the transverse velocity range is reduced, because the atoms that stay in the observation region are the slowest in the transverse direction. The density is obviously also reduced due to the divergence from the observation region.

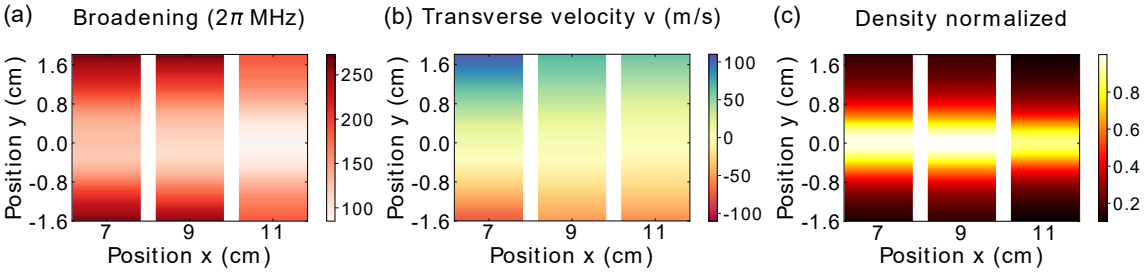

Figure 11: Two-dimensional colormaps of the the (a) broadening, (b), transverse velocity and (c) density of the atomic beam as a function of the x, y coordinates. Data obtained from measurements at positions x =7, 9, 11 cm with respect to the atomic oven.

4.1.2 Absorption

The minimum transmission $I_{\min}/I_0$ of an absorption signal is caused when the densest region is in resonance. In our case this region is the axis of the atomic beam, where atoms move mostly longitudinally. Therefore, taking into account Eq. 2, an estimation of the number of atoms per unit area the laser beam encounters moving with small transversal velocity is given by

$$n = -\frac{2\pi}{3\lambda^2} \ln \frac{I_{\min}}{I_0} \tag{6}$$

Then, we can estimate the three-dimensional density of these small transversal velocity atoms as $\rho = n/l$, where l the spatial width of the region close to resonance.

In order to acquire the absorption signal, we reduced the laser power to 65 μW to not saturate the photodiode and increased its diameter to 1.5 mm to interact with more atoms and optimize the signal. The transmission I/I_0 was obtained as the value of the

photodiode voltage reading normalized such that it is 1 far from resonance. We also correct the signal removing a slope present due to an unavoidable small power modulation of the laser when scanning.

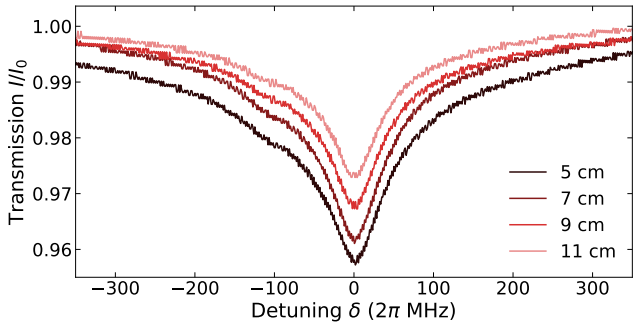

Figure 12: Absorption signal at different distances x from oven. The transmission I/I_0 is plotted as function of the detuning δ. The ^{86}Sr bump can also be observed.

Fig. 12 shows the absorption signals for different x positions. We observe how as we move away from the oven the signal gets smaller in amplitude and narrower as the density and the velocity range decrease in agreement with fluorescence results. The transmission minima are compatible with the values found in the literature for the temperature we are working with [SRG+15, Sta19, Cas20]. The minima of 0.961 (0.002) and 0.973 (0.002) at $x_1 = 7$ cm and $x_2 = 11$ cm result in longitudinally-moving atom column integrated densities of $n_1 = 3.9\ (0.3) \cdot 10^7$ atoms $\cdot$ cm^{-2} and $n_2 = 2.7\ (0.3) \cdot 10^7$ atoms $\cdot$ cm^{-2} respectively. We estimate the corresponding densities by fitting the fluorescence images at resonance to Gaussian distributions and computing the FWHMs, which give spatial lengths of the resonant region of $l_1 = 1.114\ (0.004)$ cm and $l_2 = 0.965\ (0.004)$ cm in the two positions. This values yield central densities of $\rho_1 = 3.5\ (0.3) \cdot 10^7$ atoms $\cdot$ cm^{-3} for the first position, and $\rho_2 = 2.8\ (0.3) \cdot 10^7$ atoms $\cdot$ cm^{-3} for the second position.

4.2 Longitudinal measurements

The longitudinal velocity v_l in the atomic beam axis, apart from being a key feature for the characterization of the atomic beam by itself, can be used to calculate the angle, θ, representative of the divergence. Moreover, it is also useful to estimate the central flux $\mathcal{F}$, which is the quantity that will determine the capture rate in the first trapping stage of an experiment. Measuring the longitudinal velocity in the atomic beam axis will be equivalent to measure the total velocity of these atoms. Then, the divergence angle can be estimated as $\theta = \arctan(\text{FWHM}/2v_l)$, where FWHM is the width of the transverse density distribution in velocities, and the flux of small transverse velocity atoms as

$$\mathcal{F} = \frac{N}{St} = \frac{\rho v_l t S}{St} = \rho v_l \tag{7}$$

where here N is the number of atoms that cross a transverse surface area S in a time t.

In order to measure the longitudinal velocity of the central atoms we measure their transverse velocity in a direction angled with respect to the transversal. Then, with this velocity v_α and the angle α, the longitudinal velocity can be computed as $v_l = v_\alpha / \sin(\alpha)$ (Fig. 13 (a)). However, we first need the reference in frequency of zero velocity, and therefore we need to measure the frequency at which the central atoms are in resonance for a transverse laser beam. In fact, the transverse beam serves as a reference for locating the

y position at which the broadening is minimum, and consider the atoms there as moving completely perpendicular. Then, the angle beam is aligned such that it crosses this point.

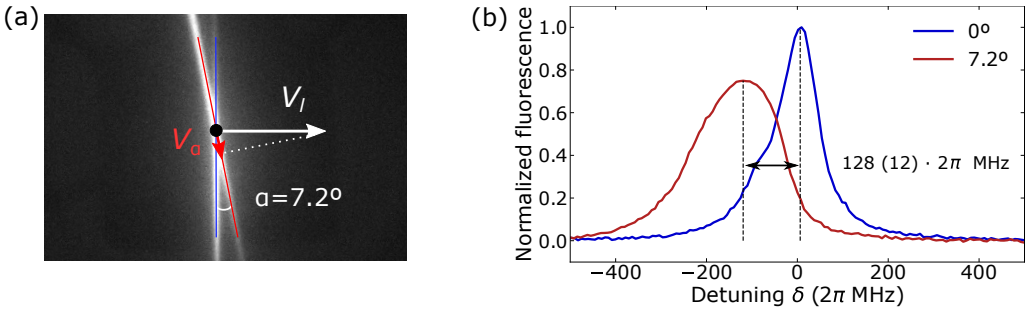

Figure 13: Longitudinal measurement sketch and results. (a) Fluorescence image of the two used beams used superimposed. The relevant parameters are highlighted. (b) Fluorescence signal at $x = 8$ cm from the oven in the center of the atomic beam for a transverse beam and beam angled 7.2°(0.01) with respect to it. The shift in frequency is displayed.

Fig. 13 (b) shows the obtained results. As we expected, the fluorescence of the angle beam shifts towards red-detuned frequencies, and also gets broader, as the velocity spread is bigger. The shift of $\Delta = 128\ (12)\ 2\pi$ MHz in frequency, corresponds to a velocity of $v_\alpha = 59\ (6)$ m/s which gives a longitudinal velocity of $v_l = 473\ (58)$ m/s. This is the most probable velocity for the theoretical distribution at 514°C, which is compatible with the temperature we read in the oven. This longitudinal velocity yields a divergence angle of $\theta = 3.63°\ (0.01)$, twice the divergence measured in [SPP+12]. The central flux obtained for the first position x_1 is $\mathcal{F}_1 = 1.7\ (0.2) \cdot 10^{12}$ atoms $\cdot$ cm^{-2}s^{-1} whereas for the second position x_2 is $\mathcal{F}_2 = 1.3\ (0.3) \cdot 10^{12}$ atoms $\cdot$ cm^{-2}s^{-1}. These results are comparable with measurements previously taken in the group's main machine, and agree with the results found in [SRG+15]. The discrepancy with the flux values of [SPP+12, SPP+12] is due to the fact that they estimate total flux, whereas we only estimate it in the central region.

4.3 Transverse cooling

With the transverse cooling configuration of the setup, we use a cooling beam a close as possible to the oven to collimate the atomic beam, and a probing beam to quantify its effect at a certain distance. First, we characterized the cooling effect as a function of the the detuning of the cooling beam, by measuring how the absorption of the probing beam fixed in resonance with the central atoms changes. This allows to obtain the optimal detuning and the enhancement in the atomic density. Then, we scanned the probing beam to generate different absorption signals for the cooling beam fixed at different frequencies. This is used to reveal the reduction in the transverse velocity, expected when collimating the atomic beam, by comparing the broadenings of the different signals.

We used the slave output with the injection lock of the commercial laser to raise the power of the cooling beam to 205 mW, and a telescope to increase its diameter to 15 mm. The distance between the cooling and probing beam, generated by the homemade laser, was set to 3 cm.

The results shown in Fig. 14 (a) showcase how the transmission of the probing beam is reduced with the cooling beam slightly red detuned, as a result of more atoms arriving at the probing position. Conversely, when the beam is blue detuned the transmission increases, indicating a density reduction. The cooling effect is found to be optimum with

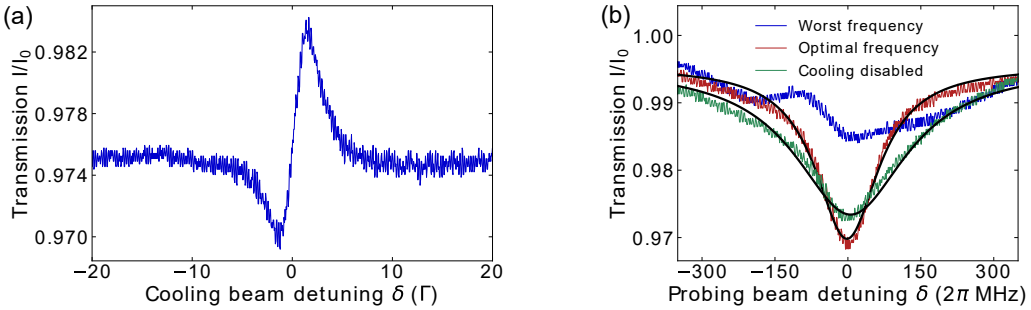

Figure 14: Transverse cooling characterization measurements results. (a) Probing beam signal on resonance under a cooling beam scan. The optimum detuning is found at $\delta = -1.2\ (0.8)\ \Gamma$. (b) Probing beam scan signal under different cooling frequencies. Lorentzian fits are shown. FWHM values are of 281 (5) 2π MHz for the cooling beam disabled and 159 (2) 2π MHz for the optimal frequency.

a detuning of $\delta = -1.2\ (0.8)\ \Gamma$. The absorption increase we obtain for this δ is of 14%, which entails a 14% increase in densities and fluxes. The probing beam absorption signals, plotted in Fig. 14 (b), agree with this result and further exhibit how, for the cooling beam at the optimum detuning, not only the absorption amplitude increases but the signal gets narrower, as expected. The reduction in the broadening, and therefore in transverse velocity, is obtained with Lorentzian fits and correspond to a 44%.

5 Conclusions and outlook

During this thesis we have constructed and characterized an atomic source. First, this includes the preparation of the vacuum system: cleaning, assembly, bake-out and strontium loading of an oven and a chamber specifically designed for its characterization. In addition, it also involves the design and construction of a full optical setup which contains a commercial and a homemade laser, a Fabry-Perot cavity, a grating wavemeter and a main setup which enables different spectroscopic measurements in fluorescence and absorption and an implementation of one-dimensional transverse laser cooling.

With the transverse measurements we have characterized the velocity and density and the transverse distributions and also estimated the central density of the atomic beam ($\rho_2 = 2.8 \cdot 10^7$ atoms $\cdot$ cm^{-3}). With the longitudinal measurement we have also inferred the longitudinal velocity on axis ($v_{\text{lon}} = 473$ m/s), which allows to obtain a diverging angle ($\theta = 3.63°$) and a central flux estimation of ($\mathcal{F}_2 = 1.3 \cdot 10^{12}$ atoms $\cdot$ cm^{-2}s^{-1}). Finally, we have characterized the cooling effect of our implementation, showing a 14% of density enhancement and a 44% reduction in the transverse velocity range.

The constructed setup also opens the possibility of performing some other interesting measurements that could complement the characterization provided. Among these, we would like to highlight the measurements at different oven temperatures and with different types of microcapillaries installed. With further processing of the data we have presented, it is also possible to consider flux models to predict the beam behaviour at the position of the experiment. In addition, our first version of transverse cooling can be further developed by optimizing the power, the position, the size and the shape of the beam, and an upgrade to a two-dimensional transverse cooling is also enabled by the chamber design.

The result of this further work together with this thesis should give insights in the effectiveness of different atomic sources designs under different operating conditions, and guide future decisions on this topic. Enhancing the atomic flux would be a major step towards increasing the efficiency of our main machine in the production of quantum gases.

Bibliography

[AGMCA+17] A. Asenjo-Garcia, M. Moreno-Cardoner, A. Albrecht, H. J. Kimble, and D. E. Chang. Exponential improvement in photon storage fidelities using subradiance and "selective radiance" in atomic arrays. *Physical Review X*, 7(3), 2017.

[BBL16] A. Browaeys, D. Barredo, and T. Lahaye. Experimental investigations of dipole–dipole interactions between a few Rydberg atoms. *Journal of Physics B: Atomic, Molecular and Optical Physics*, 49:152001, 2016.

[BC20] M. C. Bañuls and K. Cichy. Review on novel methods for lattice gauge theories. *Reports on Progress in Physics*, 83(2):024401, 2020.

[BDN12] I. Bloch, J. Dalibard, and S. Nascimbène. Quantum simulations with ultracold quantum gases. *Nature Physics*, 8:267–276, 2012.

[BDZ08] I. Bloch, J. Dalibard, and W. Zwerger. Many-body physics with ultracold gases. *Reviews of Modern Physics*, 80(3):885–964, 2008.

[Cas20] E. Casotti. A two-dimensional magneto-optical trap for strontium. Master's thesis, Ludwig Maximilians University (LMU), Munich, Germany, 2020.

[DKYB16] F Dunning, T Killian, S Yoshida, and J Burgdörfer. Recent advances in Rydberg physics using alkaline-earth atoms. *Journal of Physics B: Atomic, Molecular and Optical Physics*, 49:112003, 2016.

[Ess10] T. Esslinger. Fermi-Hubbard physics with atoms in an optical lattice. *Annual Review of Condensed Matter Physics*, 1(1):129–152, 2010.

[Est21] A. Estarellas. A 461 nm laser system for an ultracold strontium quantum gas experiment. Master's thesis, The Institute of Photonic Sciences (ICFO), Barcelona, Spain, 2021.

[Fey82] R. P. Feynman. Simulating physics with computers. *International journal of theoretical physics*, 21(6/7):467–488, 1982.

[Foo07] C. J. Foot. *Atomic physics*. Oxford master series in atomic, optical, and laser physics. Oxford University Press, Oxford, 2007.

[GAN13] I. Georgescu, S. Ashhab, and F. Nori. Quantum simulation. *Reviews of Modern Physics*, 86, 2013.

[HBS+20] L. Henriet, L. Beguin, A. Signoles, T. Lahaye, A. Browaeys, G. Reymond, and C. Jurczak. Quantum computing with neutral atoms. *Quantum*, 4:327, 2020.

[KTPO03] Hidetoshi Katori, Masao Takamoto, V. G. Pal'chikov, and V. D. Ovsiannikov. Ultrastable optical clock with neutral atoms in an engineered light shift trap. *Physical Review Letters*, 91(17), 2003.

[LBY+15] A. D. Ludlow, M. M. Boyd, J. Ye, E. Peik, and P. O. Schmidt. Optical atomic clocks. *Reviews of Modern Physics*, 87:637–701, 2015.

[Lee17] T.B.M. Van Leent. Narrow-linewidth external cavity diode lasers for atomic physicsm. Master's thesis, University of Amsterdam, Amsterdam, Netherlands, 2017.

[MCD83] J. H. Moore, M. A. Coplan, and C. C. Davis. *Building scientific apparatus: a practical guide to design and construction*. Addison-Wesley, London, 1983.

[MvdS99] H. J. Metcalf and P. van der Straten. *Laser Cooling and Trapping*. Springer-Verlag, New York, 1999.

[NM14] Pierre Nataf and Frédéric Mila. Exact diagonalization of Heisenberg SU(n) models. *Phys. Rev. Lett.*, 113:127204, 2014.

[RWE+95] L. Ricci, M. Weidemüller, T. Esslinger, A. Hemmerich, C. Zimmermann, V. Vuletic, W. König, and T.W. Hänsch. A compact grating-stabilized diode laser system for atomic physics. *Optics Communications*, 117(5):541–549, 1995.

[RWRA+20] J. Rui, D. Wei, A. Rubio-Abadal, S. Hollerith, J. Zeiher, D. Stamper-Kurn, C. Gross, and I. Bloch. A subradiant optical mirror formed by a single structured atomic layer. 2020.

[SPGS13] S. Stellmer, B. Pasquiou, R. Grimm, and F. Schreck. Laser cooling to quantum degeneracy. *Physical Review Letters*, 110(26), 2013.

[SPP+12] M. Schioppo, N. Poli, M. Prevedelli, St. Falke, Ch. Lisdat, U. Sterr, and G. M. Tino. A compact and efficient strontium oven for laser-cooling experiments. *Review of Scientific Instruments*, 83(10):103101, 2012.

[SRG+15] R. Senaratne, S. V. Rajagopal, Z. A. Geiger, K. M. Fujiwara, V. Lebedev, and D. M. Weld. Effusive atomic oven nozzle design using an aligned microcapillary array. *Review of Scientific Instruments*, 86(2):023105, 2015.

[Sta19] E. Staub. Developing a high-flux atomic beam source for experiments with ultracold strontium quantum gases. Master's thesis, Ludwig Maximilians University (LMU), Munich, Germany, 2019.

[Ste13] S. Stellmer. *Degenerate quantum gases of strontium*. PhD thesis, University of Innsbruck, Innsbruck, Austria, 2013.

[SWLY17] E. Shahmoon, D. S. Wild, M. D. Lukin, and S. F. Yelin. Cooperative resonances in light scattering from two-dimensional atomic arrays. *Physical Review Letters*, 118:113601, 2017.

[TSP18] L. Tarruell and L. Sanchez-Palencia. Quantum simulation of the Hubbard model with ultracold fermions in optical lattices. 2018.

[TYST12] S. Taie, R. Yamazaki, S. Sugawa, and Y. Takahashi. An SU(6) Mott insulator of an atomic Fermi gas realized by large-spin Pomeranchuk cooling. *Nature Physics*, 8(11):825–830, 2012.

A Vacuum preparation

The cleaning of the chamber pieces was accomplished with a 10 minute ultrasonic bath of acetone at 40°C, followed by 10 more minutes of ethanol, to clean acetone remainders. In the cases where it was necessary, the process was repeated with the pieces rotated to clean all of its surface. We also thoroughly cleaned manually some pieces which showed visible stains after the ultrasonic baths.

The assembly process was carried out using clean latex gloves, hair caps and carefully avoiding touching the inner surfaces of the pieces, which laid in clean UHV vacuum aluminum foil. We use double T nuts and M6 and M8 silver-plated bolts screwed in star-shape pattern until reaching approximately 0.4 mm of uniform separation between the two pieces of the junction. In the absence of them, we employ regular screws daubed with lubricant molybdenum-based grease to prevent thermal wear during the bake-out. The holders used consist in two custom-made aluminum pieces screwed together that clamp a selected flange, with the bottom one being screwed to standard optomechanic posts. For holding the regions that will be at higher temperature these pieces are made of stainless steel, which has a higher melting point.

To perform the bake-outs, we used 3 different heating tapes [24] connected to independent variable voltage transformers (variacs), that let us control the temperature of different regions independently and achieve a uniform heating and a smooth gradient towards the pump. Avoiding large temperature gradients is crucial to avoid opening leaks due to a different dilation of the elements in the junctions. Keeping the pump colder also facilitates the pumping of the outgassed molecules that will diffuse towards the colder regions. To monitor temperature and pressure, the thermocouples were connected to a 8-channel monitor [25] and the pressure gauge to a data acquisition device[26], that served as an interface with the computer. Everything was then wrapped in several isolation layers of aluminum foil.

For the first high-temperature bake-out we increased the temperature at 50°C/h to avoid large gradients until we reach 325°C in the cube, which was the hottest point. We baked-out at this temperature for 5 days before increasing the temperature to 400°C for 2 more days. We then cooled down the chamber at the same rate and filled it with an argon over pressure. This allowed us to replace the blanks by the viewports minimizing the atmosphere exposure. Next we preformed the second bake-out, with the viewports isolated by aluminum custom-made caps. We heated up at a rate of 7°C/h, much slower than the maximum allowed rate for the viewports, until we reached 190°C in the cube. We baked-out for 6 days, with the pressure stabilizing at $5.0 \cdot 10^{-9}$ mbar after peaking at $7.1 \cdot 10^{-7}$ mbar. We cooled down at the same rate. The pressure improvement we reached after the second baking, from $2.8 \cdot 10^{-8}$ to $2.9 \cdot 10^{-9}$ mbar, was not higher probably due to the fact that we had to perform a turbopump exchange between the two bake-outs to connect the gauge to the chamber, so the bellow was only baked-out at low temperature after atmosphere exposure. To reach this pressure we also had to tighten some screws to fix a leak that we spotted by spraying helium in the joints, which is less likely to be detected by the gauge than other heavier elements, resulting in a pressure drop if it enters through a leak displacing these other elements.

The microcapillaries were sonicated first with soap [27] diluted in deionized water, and then several times with water to remove the soap. Then we sonicated them, together with the rest of oven piezes and the tools needed for the assembly, with acetone and ethanol. With the help of a blank to support the microcapillaries we inserted them using tweezers

[24] Omega SWH251-06, STH102-060, SWH171-040 [25] Picotech TC-08 [26] LabJack T7 [27] Deconex OP 21

until the triangle aperture was filled with a regular pattern. We then clamped them with the M3 screws.

For the oven bake-out, we used nickle gaskets to closed the CF63 T we used as a baking chamber to prevent them to fuse with the blank flanges due to the high temperatures. Apart from the heating tapes, the thermocouples and the aluminum foil, we interleaved a layer of micropourus blanket isolation to help reaching the desired temperature. The temperature was increased at 50°C/h until we reached 700°C at the hottest point. We baked-out at this temperature for 4 days before cooling down. During the heating process, the pressure went from $4.5 \cdot 10^{-8}$ mbar to stabilizing at $1.2 \cdot 10^{-8}$ mbar after the 7 days of baking, with the peak pressure being $4.1 \cdot 10^{-6}$ mbar. After cooling down, the pressure dropped below the minimum pressure the gauge can read ($4.8 \cdot 10^{-10}$ mbar). With the slope of the pressure curve we estimate that it reached around $1 \cdot 10^{-10}$ mbar. We had to repeat the process a second time because the microcapillaries fell from the nozzle. We think this happened because the screws were not tight enough and the microcapillaries held together thanks to their magnetic properties that at the bake-out temperature were reduced.

In order to load the install the oven in the chamber with the strontium loaded, we filled with an argon overpressure the chamber and a plastic glovebox, were the oven pieces, the stronitum ampule and the tools required for the assembly were placed in. The glovebox was then placed around the oven side of the chamber wrapping it, sealing a safe volume full of argon. We removed the blank that replaced the oven, broke the stronitum ampule, loaded the strontium in the reservoir, placed nickle gaskets between the reservoir, the nozzle flange (with the clamp side facing the reservoir) and the connector with the main cube, and tightened the 3 pieces together with 25 mm cut screws. Once we checked that the vacuum we achieved was adequate, we removed the glovebox.

B External cavity diode lasers

Laser diodes are light-emitting diodes (LED) with a high reflectivity rear facet and a lower reflectivity front facet, forming an intrinsic cavity. Forward electrical bias across the diode junction injects electrons and holes into the depletion region that may recombine emitting photons with a large linewidth around a certain frequency that depends on the current and the temperature. The modes within this spontaneous emission linewidth compatible with the cavity will be amplified by stimulated emission as the photons travel across the junction back and forth. If the amplification overcomes the losses of the cavity, the lasing threshold is surpassed and coherent light is emitted out of the diode. In simple laser diodes this is typically the case for more than one mode.

To select and further amplify one of these modes, grating-stabilized ECDLs [RWE+95, Lee17] use a diffraction grating that for each wavelenght reflects in different directions several diffracted beams or diffraction orders, with angles that depends on the wavelength. Adjusting the grating angle, we can reflect back to the diode and amplify only the frequencies close to the target. In the usual Littrow configuration, the first-order diffraction is used for feedback while the zeroth order becomes the laser output beam. The grating also acts as a larger external cavity constraining the available modes. The resulting emission results from the combination of the spontaneous emission lineshape, the internal and external cavity modes and the dispersion of the grating. This balance is so sensitive that a small change in the grating angle, the temperature or the current of the diode can lead to suddenly amplifying an adjacent-mode, resulting in a mode-hope. Nevertheless, correctly adjusting the parameters, a smooth tuning of the frequency in a large enough mode-hope free range is possible.

C Image processing

We set the camera settings such that the signal is appreciable and the image is not saturated. Since the rate of images the programmed script can save is limited to approximately an image every 60 ms we opted to set a long scan period (30 s) to maximize the frequency resolution.

First, we took approximately 500 images over a scan period (see Fig. 9 (a)). Next, using absolute time references, we synchronized the images with their corresponding point in the piezo-electric actuator voltage signal, monitored in real-time with the computer, and selected those belonging to a semi-period that covers all the frequency range scanned. Then, another Python script is able to find the position x which displays the maximum fluorescence and crop, for each image, a narrow line around it, correcting if necessary small angles (see Fig. 9 (b)). The image with the least signal, where the laser is most off-resonance, is taken as a background and subtracted from all the images. In the cooling configuration, due to the high power, the interior of the chamber is heavily illuminated by the fluorescence of the cooling beam, resulting in a highly variable background, the effect of which cannot be completely removed to perform meaningful fluorescence measurements. Finally, all the pixels in each row are summed up leaving us with the fluorescence intensity of each y position at each detuning.

We calibrate the spatial distance in the camera by measuring the length in pixels of the top and bottom viewports and averaging the conversion factor.